

## **Multifunctional homogeneous calcium phosphate coatings: toward antibacterial and cell adhesive titanium scaffolds**

Elia Vidal<sup>1,2</sup>, Jordi Guillem-Martí<sup>1,2</sup>, Maria-Pau Ginebra<sup>1,2,3</sup>, Christèle Combes<sup>4</sup>, Elisa Rupérez<sup>1,2</sup>, Daniel Rodríguez<sup>1,2,\*</sup>

<sup>1</sup>*Biomaterials, Biomechanics and Tissue Engineering Group, Department of Materials Science and Engineering, Universitat Politècnica de Catalunya (UPC), Av. Eduard Maristany 10, 08019 Barcelona, Spain.*

<sup>2</sup>*Barcelona Research Center in Multiscale Science and Engineering, Universitat Politècnica de Catalunya, Av. Eduard Maristany 10, 08019 Barcelona, Spain.*

<sup>3</sup>*Institute for Bioengineering of Catalonia (IBEC), Barcelona Institute of Science and Technology (BIST), Baldori I Reixac 10, 08028 Barcelona, Spain.*

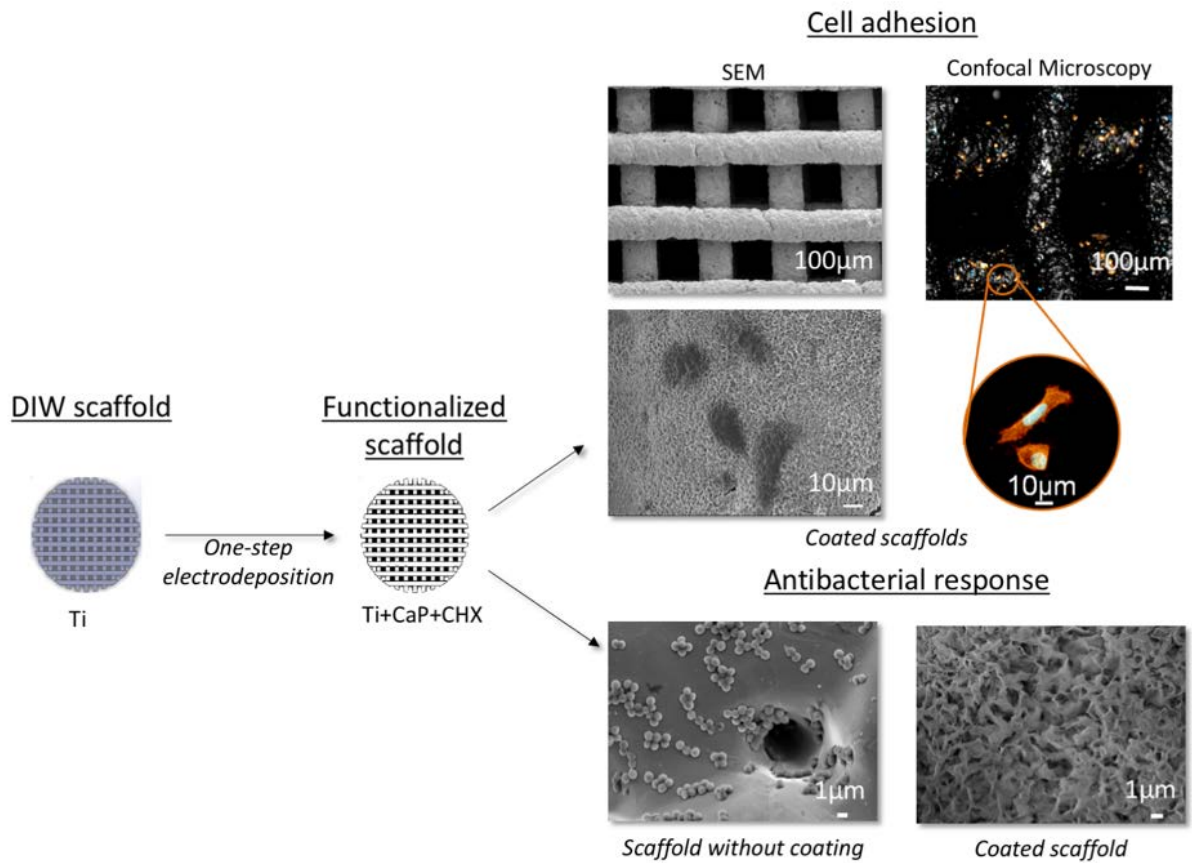
<sup>4</sup>*CIRIMAT, Université de Toulouse, CNRS, Toulouse INP - ENSIACET, 4 allée Emile Monso, CS 44362, 31030 Toulouse cedex 4, France.*

\*Author for correspondence: daniel.rodriguez.rius@upc.edu

### **Abstract**

Implants for orthopedic applications need to be biocompatible and bioactive, with mechanical properties similar to those of surrounding natural bone. Given this scenario titanium (Ti) scaffolds obtained by Direct Ink Writing technique offer the opportunity to manufacture customized structures with controlled porosity and mechanical properties. Considering that 3D Ti scaffolds have a significant surface area, it is necessary to develop strategies against the initial bacterial adhesion in order to prevent infection in the early stages of the implantation, while promoting cell adhesion to the scaffold. The challenge is not only achieving a balance between antibacterial activity and osseointegration, it is also to develop a homogeneous coating on the inner and outer surface of the scaffold.

The purpose of this work was the development of a single-step electrodeposition process in order to uniformly cover Ti scaffolds with a layer of calcium phosphate (CaP) loaded with chlorhexidine digluconate (CHX). Scaffold characterization was assessed by scanning electron microscopy, Energy dispersive X-ray spectroscopy, X-ray diffraction, micro-Raman microscopy and compressive strength tests. Results determined that the surface of scaffolds was covered by plate-like and whisker-like calcium phosphate crystals, which main phases were octacalcium phosphate and brushite. Biological tests showed that the as-coated scaffolds reduced bacteria adhesion (73±3% for *Staphylococcus aureus* and 70±2% for *Escherichia coli*). *In vitro* cell studies and confocal analysis revealed the adhesion and spreading of osteoblast-like SaOS-2 on coated surfaces. Therefore, the proposed strategy can be a potential candidate in bone replacing surgeries.



**Keywords:** Titanium scaffolds, Calcium Phosphate coating, Chlorhexidine Digluconate, Antibacterial, Biocompatibility, One-step pulse electrodeposition

## 1. Introduction

The overall rise in life expectancy has resulted in an increase in the use of medical devices such as orthopedic prostheses. These implants require an excellent osseointegration and stiffness similar to that of natural bone [1]. Titanium (Ti) has been widely used as a biomaterial due to its biocompatibility and good mechanical properties [2]. Excessive stiffness and lack of osseointegration, however, can be a problem for Ti-based implants [3].

The use of open-cell titanium structures has been considered a promising candidate in orthopedic implants to reduce the mismatch in elastic modulus between metallic implant and bone [4]. Additive manufacturing technologies based on building layer-by-layer structures with controlled geometries, such as open-cell structures, have become more accurate and more accessible [5–7]. These fabrication processes have already allowed the production of customized orthopedic implants such as acetabular cups or intervertebral discs [8].

Among the different 3D printing existing techniques, direct ink writing (DIW) fabrication process using Ti pseudoplastic inks is considered a promising methodology to build 3D Ti scaffolds at room temperature, followed by an appropriate thermal treatment. In a previous study, the preparation of such scaffolds and the optimization of the fabrication parameters were discussed [9]. The main advantage of this technique compared to powder-bed processes rests on the fact that no depowering process is needed. In consequence, post-production time, material waste, and the risk of the presence of remaining particles associated to inflammatory responses are reduced.

Another factor to consider is that Ti is an inert material. Therefore, it is ineffective for defeating infections nor promoting bone cell adhesion. Surface functionalization is one of the strategies to change surface properties such as surface bioactivity and implant-related infections.

To this end, different coating strategies have been proposed to overcome these drawbacks. One approach is to mimic the inorganic part of the bone by covering the Ti surface with a calcium phosphate (CaP) coating [10]. An existing strategy for coating Ti scaffolds is based on reverse pulsed electrodeposition, which presents several advantages compared to other coating methodologies such as plasma spraying, sol-gel or biomimetic processes [11–17]. Since the process takes place at low temperature, a higher control of the thickness and chemical composition of the coating is achieved while maintaining a high efficiency [18].

Besides, in comparison with conventional electrodeposition, the production of hydrogen bubbles deleterious to the coating formation is reduced and the ion depletion in the boundary layer close to the treated surface is avoided because of the pulses of reverse polarities [19]. It should be emphasized that, while some line-of-sight technologies such as plasma spray coating can only coat simple geometries, pulsed electrodeposition has not such limitations and can coat 3D structures, including micropores or recesses [20]. Moreover, compared with other non-line-of-sight techniques, e.g, biomimetic coating, that requires soaking the scaffold for 3 days, electrodeposition is much faster, wholly coating a surface after only 30 minutes [16].

Another important aspect related to implant osseointegration is the prevention of implant-related infections, which may produce local inflammation and eventually implant rejection. Among the different strategies, the local release of an antibacterial agent is the best alternative to systemic administration. In this regard, a CaP coating can act as a carrier for drug delivery in order to improve not only metallic implant limitations related to bioactivity but also antibacterial response by reducing bacterial colonization [21]. Several authors have reported the benefits of the adsorption of antibiotics on biomaterials surfaces. However, the use of antibiotics have to be rationalized in order to prevent microbial resistance [22, 23]. For that reason, chlorhexidine digluconate (CHX) is an antiseptic which has been used as a model of antibacterial agent [24]. It is active against an array of microorganisms, including Gram-positive and Gram-negative bacteria, and has a low risk of associated drug resistance. CHX antibacterial activity is due to the interaction of the cationic group of the molecule with negatively charged bacteria cell wall. This effect is concentration-dependent: bacteriostatic at low concentrations and bactericidal at high concentrations [25]. Furthermore, it has been shown that CaP and CHX can be co-deposited during the electrodeposition, unlike other two-steps strategies that consist on immersing CaP layer in a CHX-loaded solution [16, 26]. However, designing a one-step homogeneous coating on a scaffold surface with antibacterial response that simultaneously enhances cells adhesion remains a challenge.

In the present study a Ti scaffold, manufactured with a novel DIW technique, was functionalized with a multifunctional calcium phosphate coating with the aim to promote implant osseointegration by reducing bacterial adhesion and stimulating bone cell adhesion. The main novelty of this work was to obtain a uniform CaP coating loaded with CHX by single-step pulse reverse electrodeposition in a 3D structure. Thus, the main challenge related with the electrodeposition process was to achieve enough throughput potential to permit the layer formation inside the scaffold architecture and not only on its surface. Moreover, the concentration of CHX in the coating must be adjusted in order to combine the bioactivity of

CaP with antimicrobial effect of CHX. The biological response of the coating was tested *in vitro* with sarcoma osteogenic cells (SaOS-2) and the antibacterial activity was evaluated against both Gram-positive *Staphylococcus aureus* (*S. aureus*) and Gram-negative *Escherichia coli* (*E. coli*) models.

## 2. Materials and methods

### 2.1. Scaffolds fabrication by direct ink writing

Ti ink was prepared by mixing irregular Ti powder (~325 mesh, 99.5 % purity, Alfa Aesar, USA) with Pluronic® F127 hydrogel 30 % w/v. The development of the Ti ink and the posterior thermal treatment was previously optimized [9]. Briefly, 69 % w/w of Ti powder was mixed with 31 % w/w of Pluronic® hydrogel in a centrifuge (Speedmixer, DAC 150.1 FVZ-K) for 5 min at 3500 rpm. The resulting Ti ink was introduced in a 3 cm<sup>3</sup> syringe and placed in the 3D printing machine (Pastecaster, BCN3D Technologies, Spain). G-codes of a 0-90° pattern were loaded to the 3D printing machine in order to obtain cylindrical samples of 13 mm diameter and 5 mm height. For mechanical properties tests, samples of 13 mm diameter and 18 mm height were prepared with the same pattern. Once printed, samples were introduced in an oven for 12 h at 275 °C to eliminate the binder and finally sintered in a tubular furnace (Carbolite, UK) at 1350 °C under vacuum (10<sup>-5</sup> mbar) for 2 h.

### 2.2. Coating of the scaffolds with CaP by pulsed reverse electrodeposition

Coating of 3D printed scaffolds was performed by pulsed reverse electrodeposition. Before the electrodeposition process, scaffolds were soaked in a 5 M NaOH solution for 24 h at 60 °C to generate a thin titanate layer and finally rinsed with ultrapure water and dried in a desiccator. Calcium phosphate coatings were obtained by applying a current to the treated Ti scaffolds in an electrolyte prepared by mixing 0.042 M of Ca(NO<sub>3</sub>)<sub>2</sub>·4H<sub>2</sub>O and 0.025 M of NH<sub>4</sub>H<sub>2</sub>PO<sub>4</sub> solutions with a Ca/P molar ratio of 1.67, at pH 4.2. All reagents were analytical grade (Sigma-Aldrich, USA). The pulsed reverse electrochemical deposition was carried out in an individual cell using a three-electrode configuration in which a platinum electrode was used as an anode, a saturated calomel electrode (SCE) as reference electrode and the Ti scaffolds as cathode. Electrodeposition was conducted by using a potentiostat (PARSTAT 2273, Princeton Applied Research, Oak Ridge, TN, USA) and pulsing the current for 30 min at 40 °C [16]. A current density of 10 mA/cm<sup>2</sup> was first applied for 1 s, then current was switched off for 1.6 s (time off). Subsequently, current was regulated to -20 mA/cm<sup>2</sup> for 0.2 s and raised again to 0 mA/cm<sup>2</sup> for 0.2 s.

Samples loaded with chlorhexidine digluconate 20 % w/v (Sigma-Aldrich, USA) were prepared by adding 0.75, 1.5 and 3 mM CHX to the electrolyte solution at concentrations, hereafter named CaP+0.75mMCHX, CaP+1.5mMCHX and CaP+3mMCHX, respectively. Different concentrations of CHX were tested in order to study the minimum concentration required to have an antibacterial response. After electrodeposition process, Ti scaffolds were rinsed with distilled water and dried in a desiccator.

### *2.3. Scaffolds characterization*

Scaffolds architecture was observed by micro-computed tomography (micro-CT, SkyScan 1272, Bruker, Belgium) at a source voltage of 90 kV and current of 111  $\mu$ A, using an image pixel size of 15  $\mu$ m. Subsequently 3D reconstruction was carried out using Nrecon software (Bruker). Surface morphology of both coated and uncoated scaffolds were analyzed by scanning electron microscopy (SEM, Zeiss Neon 40, Carl Zeiss, Germany), using a working distance of 12 mm and an acceleration voltage of 5 kV. Furthermore, the coating thickness were analyzed by studying cross-sectional SEM images of three samples that were previously immersed in liquid nitrogen and fractured. Energy-dispersive X-ray spectroscopy (EDX) analyses of cryofractured samples were acquired with a FE-SEM JEOL JSM-7001F (Jeol, Tokyo, Japan) complemented with an energy dispersive X-ray spectrometer using a working distance of 10 mm and an acceleration voltage of 20 kV.

Calcium phosphate crystalline phases of the coating were identified by X-ray diffraction (XRD) using a monochromatic Cu K $\alpha$  radiation (D8 Advance Instrument, Bruker, Germany) at a scan rate of 0.25 $^\circ$ /s, in the 2 $\theta$  range of 4-45 $^\circ$  with rotation.

Moreover, coated scaffolds were analyzed using Micro-Raman spectroscopy combined with a confocal microscope (LabRam HR 800 Confocal Raman, Horiba Jobin Yvon, UK) that permitted to focus on a specific area, using a 532 nm laser, a 600 gr/mm grating and a 100X magnification objective. Acquisition of single spectrum from points of interest was performed by taking 20 accumulations of three-second integration periods. Spectra were plotted from an average of three scans of 60 s each.

Surface roughness of Ti scaffolds and CaP-coated scaffolds was observed by using a white light interferometer Wyko NT9300 Optical Profiler (Veeco Instruments, Plainview, NY, USA) in vertical scanning interferometry mode (VSI). Three measurements of the average surface roughness ( $R_a$ ) were obtained at three different zones of the scaffold, using a 10X objective lens

and a scanning area of 316 x 237  $\mu\text{m}$ . Roughness data was analyzed with Wyko Vision 4.10 software (Veeco Instruments).

The response of the scaffolds to a compressive load, with and without coating, was also evaluated. Five scaffolds ( $n = 5$ ) of 18 x 13 mm were tested for each condition using a compression testing machine (Microtest machine EM1/20/FR, Microtest, Spain) at a speed of 2.5 mm/min, in accordance with ISO 13314:2011 [27]. The elastic modulus and ultimate strength were determined from the stress-strain curves as defined in the ISO standard.

## 2.4. Antibacterial properties

### 2.4.1. Bacterial growth curve

The antibacterial activity was studied on Ti scaffolds loaded with CHX at 0.75, 1.5 and 3 mM. All antibacterial assays were performed against Gram-positive *S. aureus* (CCUG 15915, Culture Collection University of Göteborg, Sweden) and Gram-negative *E. coli* (CECT 101, Colección Española de Cultivos Tipo, Spain) bacteria, both grown in brain-heart infusion (BHI, Scharlab, Spain).

Diluted bacterial suspensions were adjusted to an absorbance of  $0.02 \pm 0.01$  at 600 nm using a photometer (Laxco MicroSpek™ DSM, USA) corresponding to a bacterial concentration of  $10^7$  colony-forming units (CFU)/mL. Then, samples were immersed in 2 mL of inoculated media using a 48 double-well culture well-plate previously prepared [28]. The antibacterial activity was monitored for 16 h by measuring absorbance at 600 nm with a multimode microplate reader (Synergy™ HTX Multimode reader, USA). Negative and positive culture controls were prepared with medium without bacteria and bacterial suspension, respectively. Ti scaffolds without coating were used as control. Moreover, for future applications of the implant *in vivo*, it is indispensable to check their stability after sterilization. In this regard, CHX-loaded scaffolds were sterilized with gamma radiation (25 kGy, Aragogamma S.L., Spain) and challenged with *S. aureus* bacterial strain in order to detect any effect of the sterilization technique on the antibacterial response.

### 2.4.2. Inhibition of bacterial adhesion

Coated scaffolds were immersed in 500  $\mu\text{L}$  of bacteria suspension previously adjusted to an absorbance of  $0.2 \pm 0.1$  ( $10^8$  CFU/mL) and incubated for 2 h at 37 °C. Then, specimens were rinsed with PBS and incubated in Alamar Blue solution (10 % v/v in medium) (AB, ThermoFisher, Belgium) for 1 h at 37 % in dark [29]. After this time, 100  $\mu\text{L}$  supernatant for

each condition were introduced in a 96 well-plate in order to measure the absorbance by using a microplate reader at  $\lambda_1 = 570$  nm and  $\lambda_2 = 600$  nm. The following formula was used to calculate the percentage difference of reduction:

$$[\frac{((\epsilon_{ox})_{\lambda_2} A_0 \lambda_1 - (\epsilon_{ox})_{\lambda_1} A_0 \lambda_2)_{test}}{((\epsilon_{ox})_{\lambda_2} A \lambda_1 - (\epsilon_{ox})_{\lambda_1} A \lambda_2)_{untreated}}] \times 100 \quad (\text{Eq.1})$$

In Eq. 1,  $\epsilon_{ox}$  is the molar extinction coefficient of Alamar Blue oxidized form ( $(\epsilon_{ox})_{\lambda_1} = 80.586$  and  $(\epsilon_{ox})_{\lambda_2} = 117.216$ ),  $A_0$  and  $A$  represent the absorbance of negative control well (media + AB without bacteria) and absorbance of positive control well, respectively. *Untreated* corresponds to untreated positive growth control and *test*, to target samples.

Finally, samples were fixed with 2.5 % glutaraldehyde in PBS for 1 h at 4 °C. Afterwards, samples were dehydrated by immersing them successively in ethanol series (50 %, 70 %, 96 % and 100 %) in order to be observed by SEM at 5 kV.

## 2.5. Cell biocompatibility

### 2.5.1. Cell adhesion

Cellular tests were performed with human osteoblast-like SaOS-2 cells (ATCC, USA) cultured in McCoy's 5A medium (Sigma-Aldrich) supplemented with 10 % v/v fetal bovine serum (FBS), 50 U/mL penicillin, 50 µg/mL streptomycin, 20 mM HEPES and 2 mM L-glutamine, all from Invitrogen.

Cell adhesion on Ti scaffold surfaces loaded with CHX was conducted at a density of  $8 \cdot 10^4$  cells/well, on quintuplicate specimens and incubated for 6 h at 37 °C, 5 % CO<sub>2</sub> in a humidified environment. After incubation, cells were lysed with mammalian Protein Extraction Reagent (m-PER, Pierce, Rockford, IL, USA). The number of attached cells was quantified by analyzing the lactate dehydrogenase (LDH) activity using the cytotoxicity detection kit LDH (Roche Applied Science, Germany). The absorbance values were measured at 492 nm with a microplate reader (Synergy™ HTX Multimode reader, USA) and then, the number of attached cells was determined using a calibration curve. Uncoated Ti scaffolds were used as controls.

Additionally, one specimen of each condition was prepared as described above, for studying cell spreading and morphology by SEM at 2 kV.

### 2.5.2. Fluorescence staining

A fluorescence staining was performed in order to study cell morphology and distribution on Ti and CHX-loaded Ti scaffolds surfaces. After 6 h incubation, cells were fixed with

paraformaldehyde 4 % w/v in PBS, permeabilized for 20 min in Triton X-100 0.1 % w/v in PBS in order to allow the molecules diffusion into the cell, and finally a blocking step was conducted by immersing the specimens in bovine serum albumin (BSA 1 % w/v in PBS) for 30 min. Alexa Fluor 546 Phalloidin (1:300 in triton 0.05 %) was used to stain actin filaments for 1 h and 4',6-diamidino-2-fenilindol (DAPI 1:1000 in PBS-glycine 20 mM) for 2 min to stain the nuclei, both in the dark. Specimens were washed with PBS-glycine solution three times for 5 min, between each step. Specimens were mounted with Mowiol 4-88 (Sigma-Aldrich) and visualized using a Zeiss LSM 800 confocal microscope (Carl Zeiss, Jena, Germany). A laser emission at 640 nm was used to obtain a reflection image of the scaffold.

### *2.6. In vitro drug release*

CHX release studies were carried out by immersing scaffolds loaded with CHX in 1 mL of Tris(hydroxymethyl)methylamine buffer solution (TRIS, VWR International Ltd., UK) at physiological pH, for 14 days and 37 °C, under SINK conditions (sufficient media is present in relation to the drug to be dissolved). At each time point, all solution was removed and replaced by new medium. For the quantification of the CHX released, absorbance was measured with a UV-spectrophotometer ( $\lambda = 254$  nm; Shimadzu model 3600, Tokyo, Japan). Triplicates of each condition were used. Moreover, in order to calculate the percentage of released CHX at each time point, the real amount of loaded CHX was obtained by adding released and unreleased values of CHX. To this end, unreleased CHX was quantified by immersing a sample from the final time point in 1 mL of HNO<sub>3</sub> 0.1 M and subsequently determining the amount of CHX that remains in the coating using the corresponding calibration curve.

CHX release profile was studied by using different mathematical models (Korsmeyer-Peppas model and Kopcha).

### *2.7. Statistical analysis*

All data presented in this study are given as mean value  $\pm$  standard deviation. At least triplicate samples (n = 3) were used for statistical analysis, except for compression test study and cell adhesion assay where five samples were analyzed. A non-parametric Kruskal-Wallis test followed by Mann-Whitney test with Bonferroni correction was used to determine the statistically significant differences ( $p < 0.05$ ) between group means.

### 3. Results and discussion

#### 3.1. Scaffolds characterization

Micro-CT reconstruction of the obtained scaffolds, as well as SEM micrographs are presented in Figure 1. The surface of scaffolds without coating showed the presence of neck formation between particles produced during the sintering. Interestingly, SEM images of coated scaffolds revealed the presence of a homogeneous CaP coating which also covers the internal architecture and even the open pores of the scaffold (Fig. 1D). Cross-section measurements resulted in a coating thickness of  $10.1 \pm 0.6 \mu\text{m}$ . Coating homogeneity was probably achieved by working with pulsed reverse current during the electrodeposition process, which reduces hydrogen gas generation at the cathode surface and enhances the ion penetration in the 3D scaffold. It is important to highlight that the coated area inside the scaffold will be protected against shear stress during implant insertion as it will not be in contact with the surrounding tissues.

Analyzing in detail the surface morphology, three different crystal morphologies are observed: a region with large platelet-like crystals of around  $30 \mu\text{m}$  in length, another with platelet-like crystals of  $15 \mu\text{m}$  and an area composed of needle-like crystals of approximately  $5 \mu\text{m}$  in length (Fig. 1C). Roughness of the surface may be affected by this grain size of the CaP crystal structure. However, although coated scaffolds showed a higher roughness ( $R_a = 5.6 \pm 0.7 \mu\text{m}$ ), the difference with non-coated surfaces is not significant ( $R_a = 5.3 \pm 0.3 \mu\text{m}$ ) probably because the original 3D scaffold roughness is quantitatively higher than the increased roughness due to the coating.

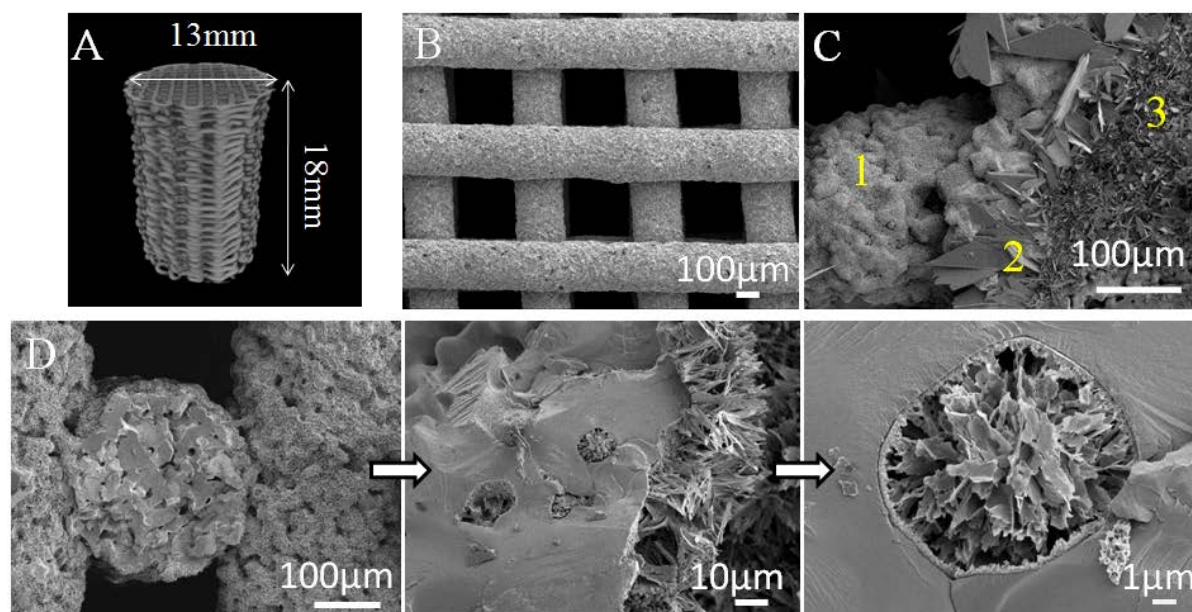


**Figure 1.** A) Micro-CT image reconstruction of a Ti scaffold (type of scaffolds used for the compression test), B) SEM image of the scaffold printed using a 90° pattern, C) Representative SEM image of coating morphology, three different zones are shown: 1) needle-like area, 2) platelet-like crystals of around 30 μm and 3) smaller platelet-like crystals of around 15 μm, and D) SEM images of the cross-section of the coated scaffold with a higher magnification image of an open pore covered and filled with calcium phosphate.

An EDX mapping of a cryofractured Ti scaffold (Fig. 2A), showed mostly the presence of titanium on both the external surface and the freshly created fractured surface, with only a minor presence of C in the surface on the strut, as reported in a previous characterization of these type of scaffolds [9]. In contrast, the EDX mapping of a cryofractured coated scaffold (Fig. 2B) reported a homogenous coating of Ca, P and O only on the external surface of the strut. Besides, since no Ti was detected on the surface of the strut, but only on the cryofracture, the coating must be some micrometres thick, corroborating the previously commented SEM measurements.

A detailed observation of the coated scaffold revealed zones with the presence of large crystals, as those seen in point 2 of Fig. 1C. The EDX mapping of one of these areas (Fig. 2C) clearly distinguished two regions with respect to the phosphorus presence (and for extension to the Ca/P ratio), one for the large crystal and the rest for the area with smaller crystals. In order to quantify this effect, Ca/P ratios were calculated from EDX spot measurements carried out on both the large and the small crystals (points 1 and 2 in Fig. 2C). The Ca/P ratios calculated from the EDX spectra were  $\text{Ca/P} = 1.30$  for point 1 and  $\text{Ca/P} = 0.95$  for point 2, respectively (Supplementary information, Fig. S1 and Table S1). Both ratios are close to those expected for

an octacalcium phosphate ( $\text{Ca/P} = 1.33$ ) and brushite ( $\text{Ca/P} = 1.0$ ) [30]. Considering the semi-quantitative nature of the EDX ratio estimations, however, other techniques are required to confirm the phases present in the coating.

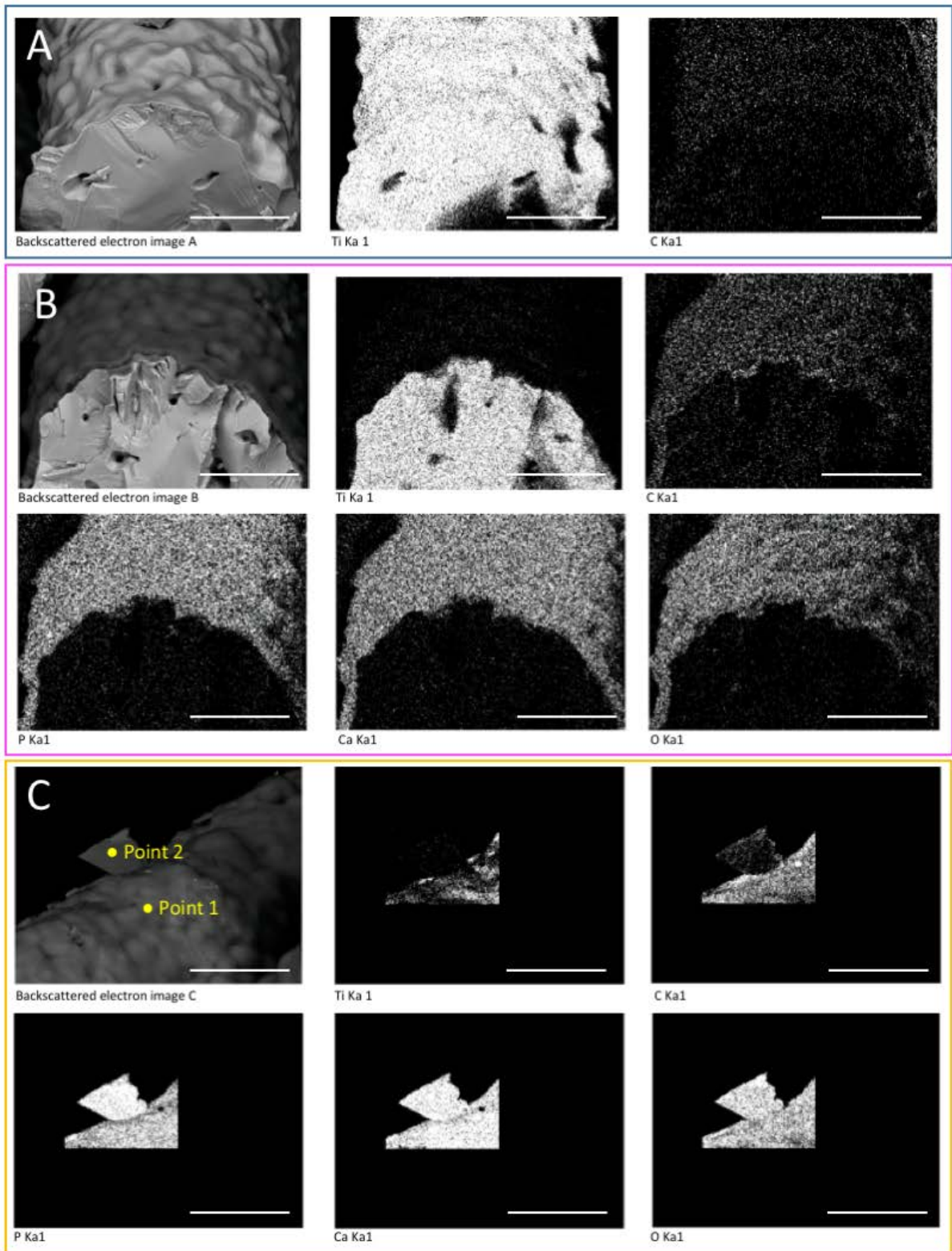
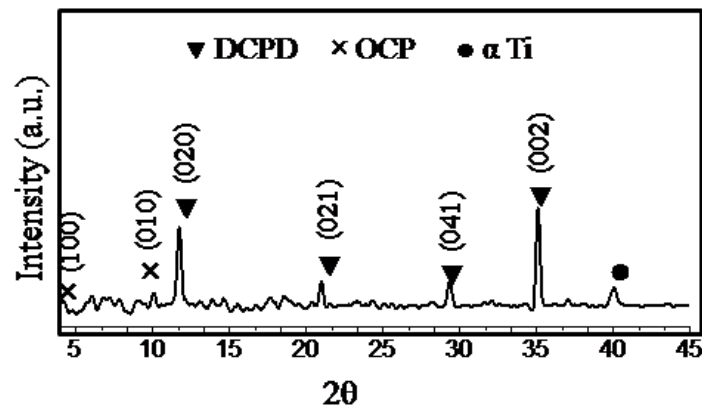


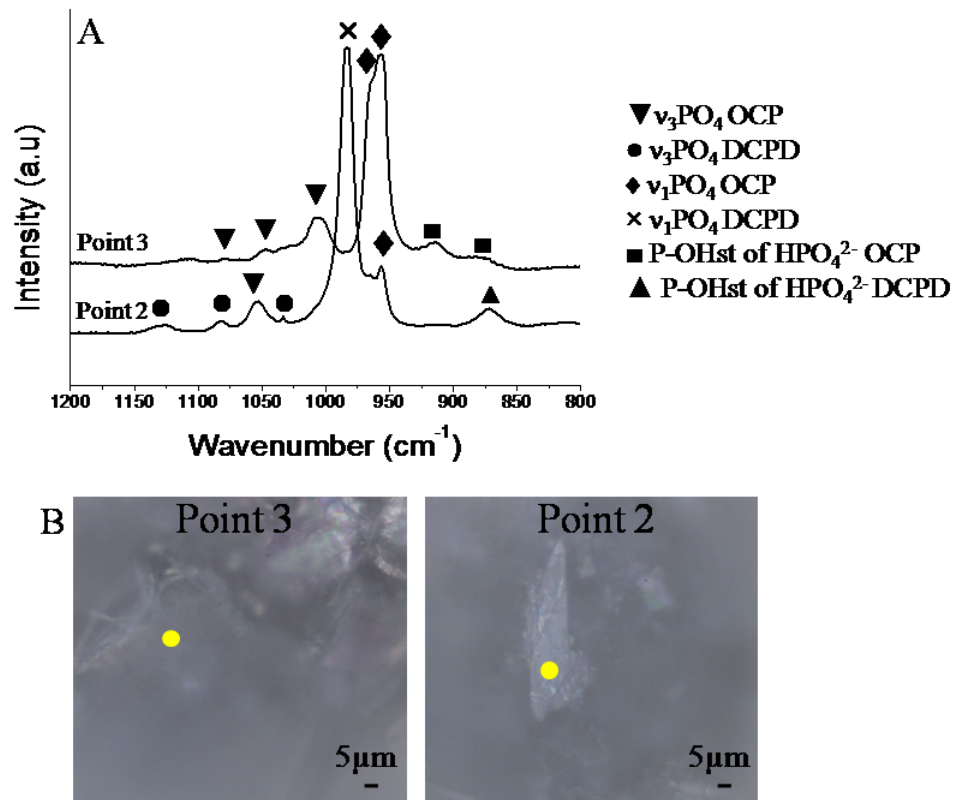
Figure 2. EDX mapping of cryofractured samples: A) Ti scaffold, B) CaP-coated Ti scaffold and C) detail on the surface on the coated Ti scaffold with different crystal morphologies. Scale bar: 100µm.

To further confirm the crystallography of the observed structures, XRD data of a coated scaffold was studied (Fig. 3). Results revealed the presence of sharp peaks assigned to brushite phase (DCPD,  $\text{CaHPO}_4 \cdot 2\text{H}_2\text{O}$ , according to JCPDS no. 72-0713 brushite standard) and small peaks that may be attributed to octacalcium phosphate phase (OCP,  $\text{Ca}_8(\text{HPO}_4)_2(\text{PO}_4)_4 \cdot 5\text{H}_2\text{O}$ ), according to JCPDS no. 79-0423 octacalcium phosphate standard). However, strong diffuse background, especially at low diffraction angles may hamper the identification of this phase. It is worthwhile to mention that the peaks relative intensity can differ from standard patterns since in electrochemical deposition crystal growth perpendicularly to scaffold surface is favored. Even though, these results strengthen the hypothesis suggested by the EDX analysis concerning the type of crystals present in the CaP coating. Peaks associated to the alpha titanium substrate were also detected (JCPDS card no. 89-2762).



**Figure 3.** XRD pattern of a coated scaffold. ▼ : Brushite (DCPD); x: Octacalcium phosphate (OCP); ● :  $\alpha$ -Titanium ( $\alpha$  Ti).

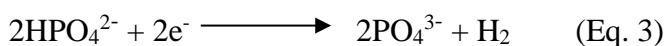
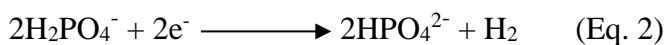
Micro-Raman spectroscopy was used to obtain complementary information to XRD results (Fig 4). For point 3 in Fig. 1C, the strongest peaks were observed at  $\approx 958$  and  $966 \text{ cm}^{-1}$  which correspond to characteristic bands of the  $\nu_1 \text{ PO}_4^{3-}$  vibration mode in OCP. For point 2 (Figs. 1C and 4B), the strongest peak was observed at  $\approx 986 \text{ cm}^{-1}$  which is characteristic of DCPD. Moreover, for point 2 a peak of around  $966 \text{ cm}^{-1}$  was also present, which means that small crystals of OCP are covered by bigger crystals of brushite, as shown in point 2 (Figs. 2C and 4B) [31]. This result can shed some light on the mechanism of CaP formation on the scaffold surface.

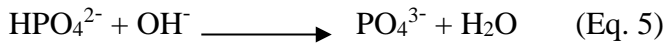
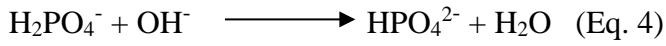


**Figure 4.** A) Raman spectra of coated scaffolds in 800-1200  $\text{cm}^{-1}$  domain, two points of interest were analyzed B) crystals area corresponding to point 2 and 3 observed in the SEM image (Fig. 1 C).

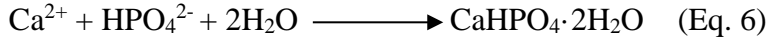
These results confirmed the XRD results and are also in agreement with the phases obtained by several authors that have characterized the calcium phosphate phases obtained from an electrochemical process [32, 33]. The presence of these phases might favor bone ingrowth around the coated scaffold due to their potential as precursors of hydroxyapatite formation [34].

Several electrochemical and chemical reactions take place during the electrochemical deposition. The CaP deposition on the scaffold surface is due to the pH-dependent solubility of CaP phases during the electrodeposition process. First, water and/or oxygen reduction near the cathode leads to hydroxyl ions generation that locally increases the pH [35]. Subsequently, according to literature, formation of  $\text{PO}_4^{3-}$  anions can occur due to the reduction of  $\text{HPO}_4^{2-}$  and  $\text{H}_2\text{PO}_4^-$  (Eq. 2 and 3) or also produced chemically as the concentration of  $\text{OH}^-$  increases in the electrolyte (Eq. 4 and Eq. 5) [36].





DCPD is stable for  $\text{pH} < 5.5$ . For that reason, it is likely to be the first CaP phase to be deposited (Eq. 6):



At the first stage of electrodeposition, the concentration of  $\text{OH}^-$  is probably not sufficient to convert  $\text{HPO}_4^{2-}$  into  $\text{PO}_4^{3-}$ , thus reactions Eq. 2, 4 and 6 will be the predominant ones.



When the concentration of  $\text{OH}^-$  is increased, OCP could precipitate easier than DCPD according to reactions Eq. 3, 5 and 7. Thus, the abovementioned mechanism could explain the presence of both OCP and DCPD phases observed by SEM and micro-Raman.

Scaffolds mechanical properties were evaluated testing scaffolds with and without CaP coating. The measured Young's modulus and compressive strength values were statistically comparable between both groups, illustrating that the coating process did not change the mechanical properties of the scaffold (Fig. 5).

Besides, Young's modulus values are higher than those measured in previous studies ( $0.63 \pm 0.01$  GPa) [9]. The differences may be attributed to differences in the sintering process. In this work scaffolds were sintered under vacuum instead of Ar atmosphere. One sintering mechanism is the evaporation/condensation, which is more effective when sintering under vacuum. For that reason, this mechanism have more relevance when sintering under vacuum and thus the densification of the scaffold is improved by pore movement during grain coarsening when compared to sintering in Ar atmosphere [37]. Moreover, sintering under Ar atmosphere can lead to gas trapped in closed pores that will also reduce densification [38].

The measured Young's modulus of the scaffolds were similar to those of cancellous human bone. It has been reported that cancellous bone with porosity of 50-90% and pores of 200-600  $\mu\text{m}$  possesses Young's modulus of 0.3-3.0 GPa [39]. Concerning to ultimate strength results, the measured values were closer to those described in the literature for human cancellous bone

(~40MPa) than to cortical bone (~190MPa) [39, 40]. Therefore, the tested scaffolds, with a porosity of 73.9%, may be considered as potential substitutes for human cancellous bone [9].

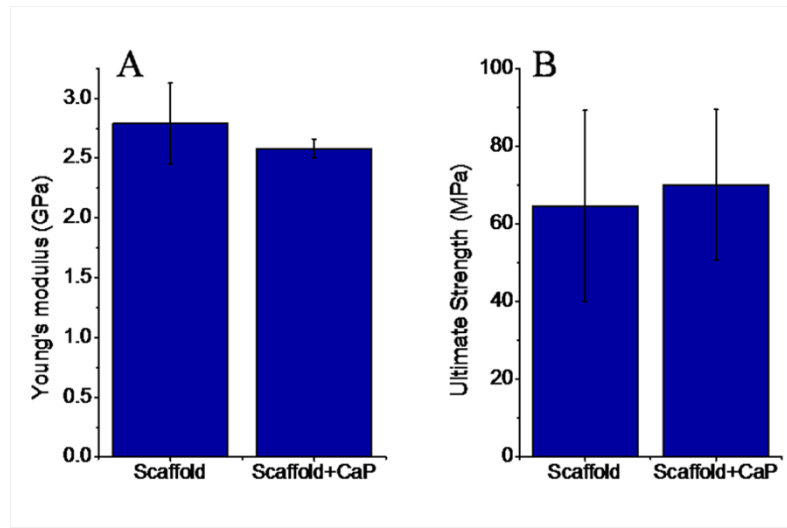


**Figure 5.** Mechanical properties of CaP-coated and non-coated scaffolds: A) Young's modulus and B) Ultimate strength.

### 3.2. Antibacterial response

Concerning the antibacterial activity, the response of the CHX-loaded CaP coating against two bacteria strains was analyzed. The optimal concentration was defined as the one that inhibits bacteria proliferation of Gram-positive and Gram-negative bacteria. To this end, increased concentrations of CHX were added to the electrolyte solution implemented to coat the porous scaffold and bacteria growth was monitored for 16 h. Results showed that for *S. aureus* all the tested concentrations avoided bacteria proliferation (Fig. 6A). For *E. coli*, however, concentrations above 0.75 mM were needed (Fig. 6B). For this reason, 1.5 mM was determined as the minimal CHX concentration required for inhibition of both bacteria growth.

In order to check any effect of a gamma irradiation sterilization process on the antibacterial activity, the antibacterial test with *S. aureus* was repeated with  $\gamma$ -irradiated scaffolds. Figure 6C revealed that bacteria in contact with CHX-loaded scaffolds did not grow. This result confirmed that the antibacterial potential of the CHX molecule was not altered by the gamma radiation.

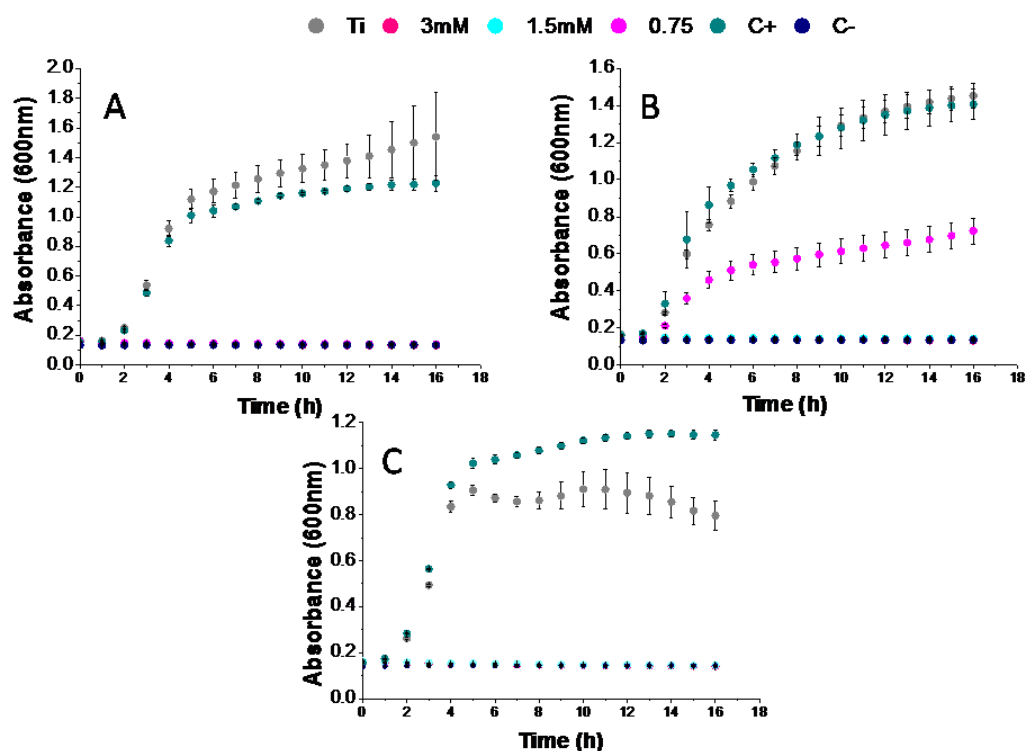


**Figure 6.** Bacteria growth curves: A) *S. aureus*, B) *E. coli* and C) *S. aureus* after scaffold sterilization with gamma radiation.

Once determined the optimal CHX concentration, 0.75 mM for *S. aureus* and 1.5 mM for *E. coli*, the next step was to evaluate the bacteria attachment. To this end, Alamar Blue assays were performed to investigate initial bacteria adhesion, which is the previous step before biofilm formation. As shown in Table 1, the presence of a higher concentration of CHX in the electrolyte solution increased the antimicrobial effect. Results showed that CHX is more effective against Gram-positive bacteria than Gram-negative ones. This different response has been previously reported in literature and can be attributed to the presence of an outer cell wall membrane in Gram-negative bacteria [41]. This outer cell wall membrane functions as a physical barrier that gives higher resistance. In contrast, Gram-positive bacteria are more sensitive to CHX probably due to the lack of this outer membrane [25].

**Table 1.** Antibacterial activity of functionalized scaffolds expressed as % of reduction of bacteria adhesion in regards to bare Ti scaffolds.

| Conditions   | Inhibition of bacteria adhesion (%) |                |
|--------------|-------------------------------------|----------------|
|              | <i>S. aureus</i>                    | <i>E. coli</i> |
| CaP+1.5mMCHX | 73 ± 3                              | 70 ± 2         |
| CaP+3mMCHX   | 82 ± 2                              | 75 ± 2         |

These findings are in accordance with the measured growth curves, where a concentration of 0.75 mM was sufficient to inhibit *S. aureus* bacteria growth, in contrast with *E. coli*, where this concentration need to be doubled. SEM images of uncoated Ti scaffolds (control) and CaP coated scaffolds without CHX showed the presence of bacteria (Fig.7 from A to F).

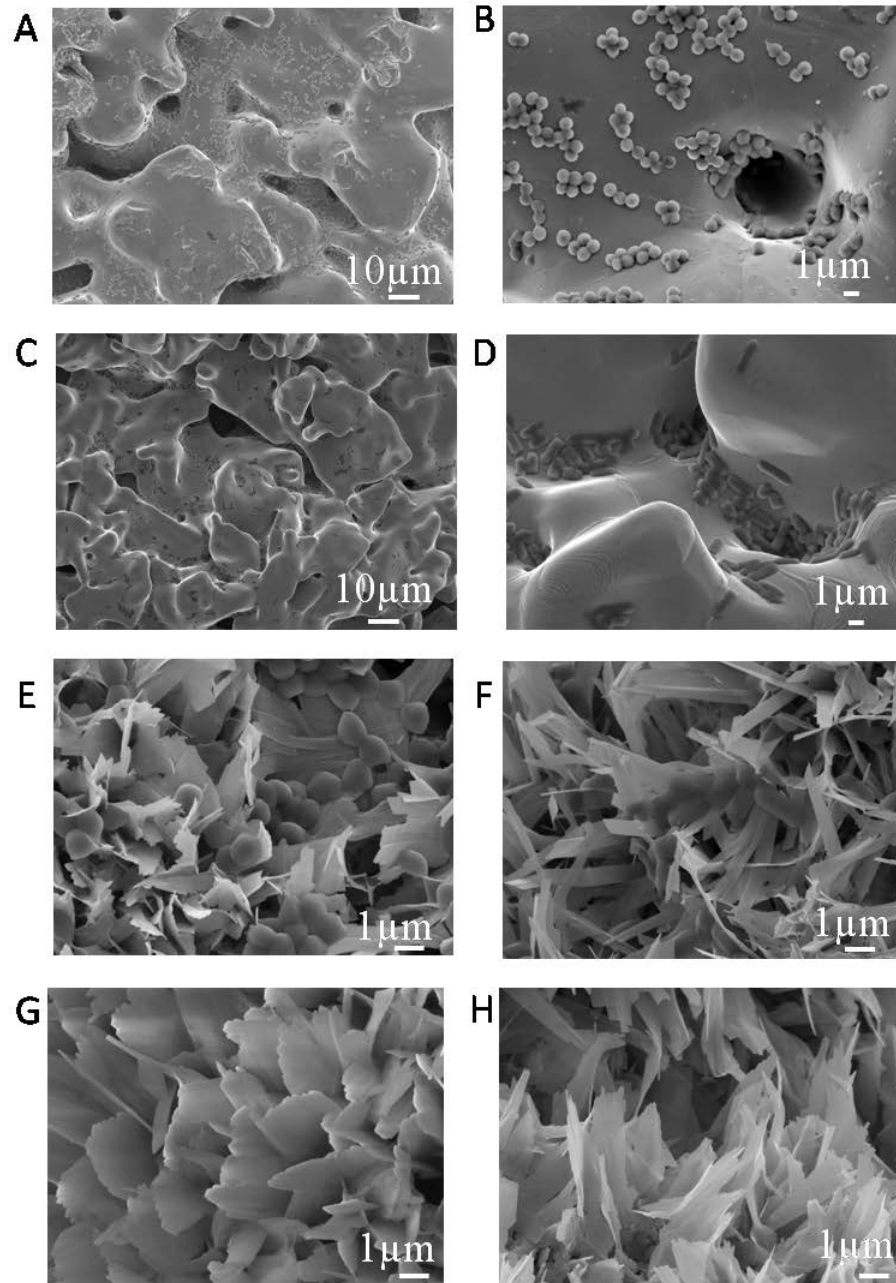


**Figure 7.** SEM images of: Ti scaffolds without coating tested against *S. aureus* (A and B) and *E. coli* (C and D). SEM images of CaP coated surfaces without CHX exposed to E) *S. aureus* and F) *E. coli*. Finally, scaffolds coated with CaP+1.5mM CHX tested against G) *S. aureus* and H) *E. coli*.

### 3.3. Osteoblast-like behavior on biofunctionalized surfaces

#### 3.3.1. Cell adhesion

After the study of the antibacterial properties, the effect of the presence of CHX on SaOS-2 cells was evaluated. It has been reported in literature that CHX is cytotoxic *in vitro* when SaOS-2 cells are exposed to concentration of CHX (0.01 %, in medium) for 1 min [42]. For that reason, to observe the osteoblast-like SaOS-2 cells behavior in contact with functionalized scaffolds, samples were incubated for 6 h and the number, spreading and morphology of adhered cells was evaluated. Results showed that cell adhesion on the surface of scaffolds loaded with 1.5 mM of CHX into the electrolyte solution was statistically similar to that of Ti scaffolds without coating (Fig. 8A). These values were statistically lower compared to scaffolds coated with CaP without CHX. Although the capacity of SaOS-2 cells to adhere to the CaP surface is reduced when the coating is loaded with 1.5 mM of CHX, the effect of the presence of CHX is probably compensated by the cell adhesion potential showed on CaP coating [26].

Cells spreading and morphology were further studied in terms of cell area (Fig. 8B). These studies revealed that cells spreading was significantly promoted on CaP and CaP+1.5mM coatings, compared to Ti scaffolds (control). In contrast, higher concentrations of CHX (3 mM in the electrolyte solution) yielded a reduction of both cell adhesion and cell spreading.

Finally, SEM and fluorescence images were used to visualize cells on scaffolds surface (Fig. 8C and 8D). SEM images corroborated the results reported previously. Increasing the CHX concentration from 1.5 mM to 3 mM yielded to a reduction in cell adhesion and spreading. For that reason CaP+1.5mMCHX condition was considered the optimal for reaching a compromise between cell adhesion and antibacterial response.

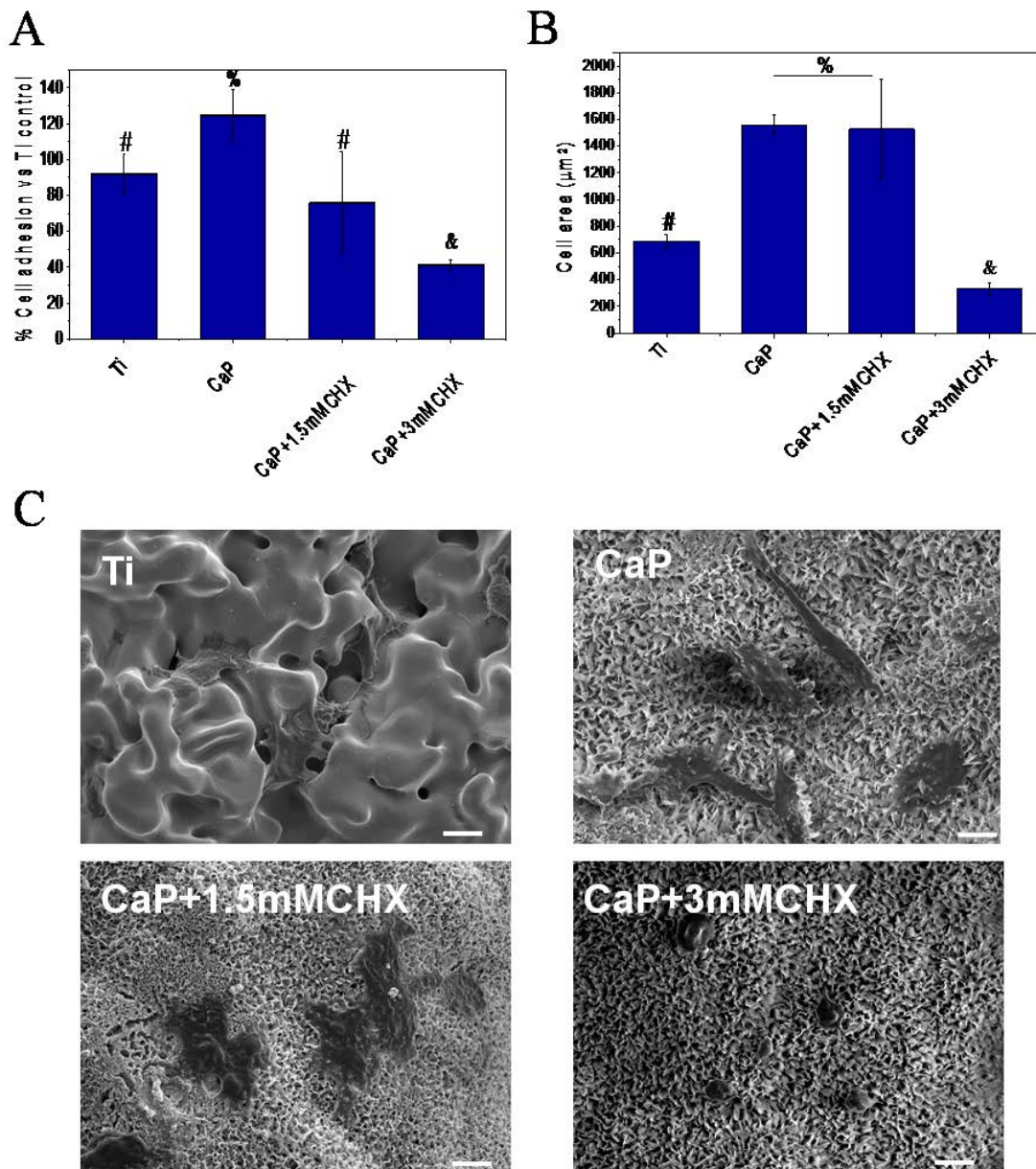


**Figure 8.** A) Adhesion and B) cell spreading of SaOS-2 cells on Ti and functionalized Ti scaffolds. C) SEM images of Ti and coated surfaces after 4 h incubation (scale bar 100 µm). Symbols (#, % and &) indicate statistically significant differences ( $p < 0.05$ ).

### 3.3.2. Confocal imaging analysis

Even though the difficulty of acquiring confocal imaging of opaque samples, images were obtained by confocal microscopy taking the advantage of the Ti and CaP crystals light reflection on the prepared scaffolds. The images revealed how cells were distributed on treated and untreated samples (Fig. 9). Combining both images offer a valuable information about cell distribution on Ti scaffolds. Interestingly, cells were more prone to adhere throughout the

surface of the coated filaments of the scaffolds without CHX in comparison with uncoated scaffolds, where cells were attached to the lateral part of the rods (Fig. 9A and 9B). This can be due to a dual effect that may occur during cells seeding. Coated surfaces may facilitate cell anchoring due to both chemical interactions and coating morphology [43].

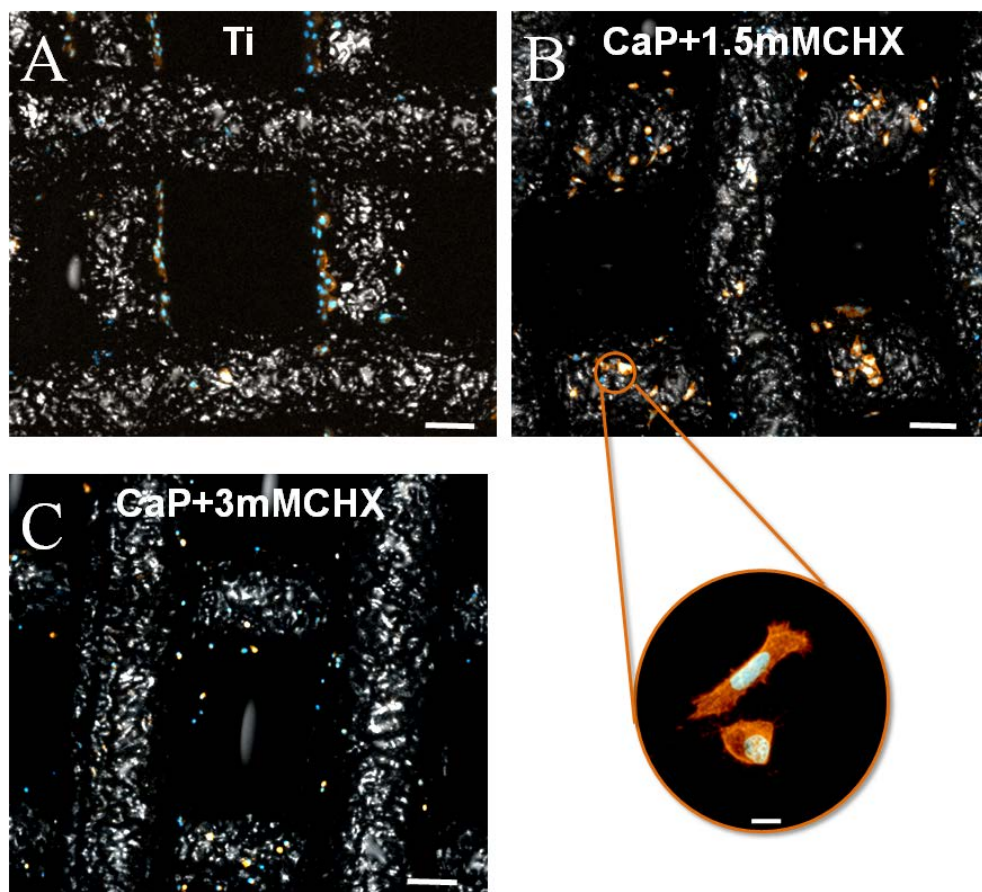


**Figure 9.** Representative images obtained by confocal microscopy of stained SaOS-2 cells on A) Ti scaffolds, B) CaP+1.5mM CHX and C) CaP+3mM CHX scaffolds. Scale bar 100  $\mu\text{m}$  (10  $\mu\text{m}$  for the circular insert image).

Higher magnification images (e.g. Fig. 9B circular insert) confirmed that for the CaP+1.5mMCHX condition, cells are spread, which means that this CHX concentration does not inhibit cell adhesion.

### 3.4. *In vitro* drug release

Once the antibacterial properties and the cell-adhesive response of scaffolds loaded with 1.5 mM CHX were tested, efforts were focused on studying the release behavior of this condition. The total amount of CHX loaded to the coating was found to be  $136.8 \pm 1.6 \mu\text{g/mL}$ . This amount is significantly higher than the CHX loading measured in a previous research where smooth Ti surfaces were functionalized with a similar CaP coating, with a total amount

of  $45 \pm 19 \mu\text{g/mL}$  CHX loaded in the coating [16]. The higher concentration of CHX on Ti scaffolds may be a consequence of the increased current density in the pulsed electrodeposition and the increased specific area of the scaffold when compared to the previous study, promoting a higher CHX loading.

Because of the increased CHX presence in the coating, when comparing the bacterial growth curves obtained in the present study (Fig. 6) with those reported on smooth Ti surfaces [16], only half of the concentration of CHX is required in the electrolyte in order to load enough antiseptic in the coating for inhibiting bacterial growth. Besides, the release of CHX maintains antibacterial concentrations for more than 14 days (Fig. 10B), a significant improvement when compared to the previous study, where samples released more than 80% of the CHX in less than 6 days. This result is even more significant when considering that a high surface roughness (as that of the present Ti scaffolds) is more suitable for microbial colonization [44].

The cumulative release curve presented a burst release for the first 12 h with 52 % of CHX released (Fig. 10A). Since most surgical infections are believed to occur during the first 6 h after implantation, these results may ensure a noteworthy effect against implant associated infection [45]. More than 1 week afterwards, CHX was still released from the coating although the increase was less pronounced.

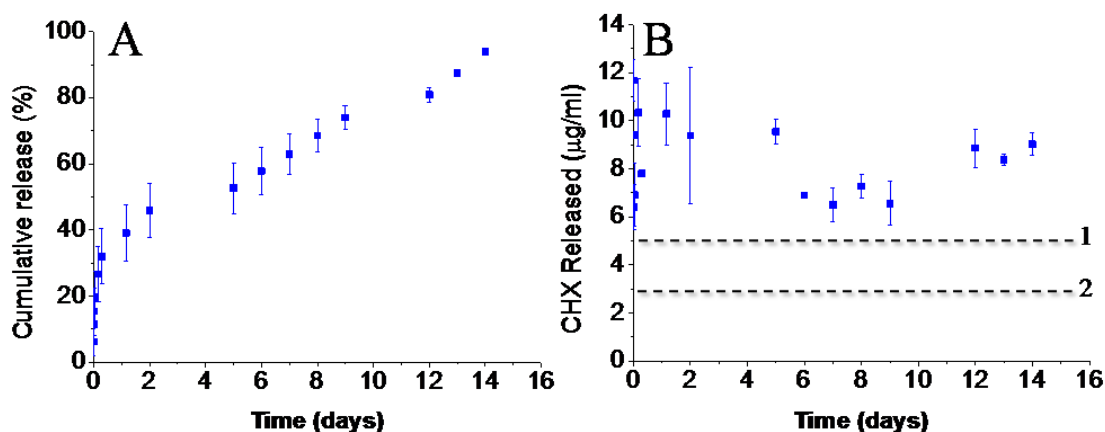


**Figure 10.** A) Cumulative release of CHX from CaP+1.5mMCHX scaffolds and B) CHX released at each time point. Broken lines show CHX MIC values for (1) *E. coli* and (2) *S. aureus*.

In order to understand the release mechanism involved, different models were applied to the first 60 % of the CHX release curve.

Korsmeyer-Peppas model (KP) can be used to study the limiting drug release mechanism [46,47]. To this end, the concentration of drug released was correlated to Eq. 8, where  $M_t$  is the drug amount released at time  $t$ ,  $M_\infty$  is the maximum amount released from the coated scaffold,  $k$  is a constant incorporating structural and geometric characteristics of the drug dosage form, and  $n$  is the released exponent that is characteristic of the limiting transport mechanism. Values of  $n$  lower than 0.5 is attributed to pseudo-Fickian diffusion, whereas values from 0.5 to 1.0 correspond to non-Fickian transport [48].  $M_t/M_\infty$  was obtained for each specimen and averaged for each condition [49].

$$M_t/M_\infty = kt^n \quad (\text{Eq. 8})$$

Results from KP model showed that the value of  $n$  was lower than 0.5 showing that pseudo-Fickian diffusional mechanism controlled the release of CHX from coating (Table 2) [50]. However, since resulting squared multiple correlation coefficient  $R^2$  for KP model was relatively low, it was necessary to deepen the understanding of the mechanisms of CHX release by studying another model as Kopcha.

Kopcha model can provide insights regarding the contribution of the diffusion (A) and erosion (B) mechanisms. When the calculated ratio A/B is higher than 1, the contribution of the diffusion is predominant (Eq. 9).

$$M_t = At^{0.5} + Bt \quad (\text{Eq. 9})$$

In this model, the A/B ratio obtained showed that although the presence of the erosion phenomena, it is the diffusion mechanisms that prevail and lead to the release of CHX [50]. Moreover, this model provided a better goodness of fit for the studied condition (Table 2).

**Table 2.** Parameters obtained from Korsmeyer-Peppas and Kopcha modelling of CHX release from CaP+1.5mMCHX samples.

|              | Korsmeyer-Peppas model |                | Kopcha model |                |
|--------------|------------------------|----------------|--------------|----------------|
|              | n                      | R <sup>2</sup> | A/B          | R <sup>2</sup> |
| CaP+1.5mMCHX | 0.25                   | 0.954          | >>1          | 0.971          |

The amount of CHX released at each time point was found to be always above the MIC of *S. aureus* (3 µg/mL) and *E. coli* (5 µg/mL) (Fig. 10B)[25]. This is a relevant result, since

sub-MIC doses can lead to the risk of resistance. It worth mentioning that the protocol to quantify the CHX release was based on the total replacement of the medium at each time point. Replacement of total medium produces a higher gradient of concentration closed to the substrate compared to replacing only half of the medium. J. Barros et al. studied this effect on CHX-loaded nanohydroxyapatite by adsorption, and observed slower release kinetics when only half of the medium was replaced [25]. Thus, it is important to highlight that for electrochemical co-deposition strategy, even with a total replacement protocol a sustained released is achieved above the MIC of both bacteria strains. Moreover, regarding the loading process, it is worth mentioning that adsorption strategies are performed in two steps, first the calcium phosphate layer is prepared and subsequently samples are immersed in a solution of CHX. For that reason, the complete process can take place in several hours [25], [51]. In contrast, the present study described a one-step process where during the formation of CaP layer, the CHX is co-deposited. More specifically, the loaded coating can be produced in only 30 minutes.

#### **4. Conclusion**

In this work, DIW printed scaffolds have been manufactured with improved mechanical properties compared with previous studies. Moreover, scaffolds have been successfully coated with a pulsed electrodeposition process achieving a uniform CaP layer both on the inner and outer the surface of the scaffold. In addition, biofunctionalized scaffolds demonstrated antibacterial activity against Gram-positive and Gram-negative bacteria strains, even after  $\gamma$ -irradiation. Cell culture tests also showed that CHX-loaded scaffolds presented a cell adhesion similar to that of Ti scaffolds.

Therefore, the proposed strategy can efficiently improve orthopedic implants in terms of reaching bone-like and biointegration properties while reducing infections around the implant.

#### **Acknowledgments**

The authors thank the Generalitat de Catalunya financial support (SGR 2017 SGR1165), the Spanish Government for financial support through project RTI2018-098075-B-C21 (MINECO/FEDER), co-funded by the EU through European Regional Development Funds, BIOACTISURF project no. 14054394 of the Midi-Pyrénées Region and COST Action Ipromedai TD1305. EV acknowledges the FI-DGR scholarship and MPG the ICREA Academia Prize, both by the Generalitat de Catalunya.

## References

- [1] S. Wu, X. Liu, K.W.K. Yeung, C. Liu, X. Yang, Biomimetic porous scaffolds for bone tissue engineering, *Mater. Sci. Eng. R Reports*, 80 (2014) 1–36.
- [2] M. Geetha, A. K. Singh, R. Asokamani, A. K. Gogia, Ti based biomaterials, the ultimate choice for orthopaedic implants - A review, *Prog. Mater. Sci.*, 54 (2009), 397–425.
- [3] W. Wang, C.K. Poh, Titanium Alloys in Orthopaedics, in: J. Sieniawski (Ed.), *Titanium Alloys - Advances in Properties Control*, IntechOpen, 2013, pp.1–20.
- [4] B.D.C. Dunand, Processing of Titanium Foams, *Adv. Eng. Mater.*, 6 (2004) 369–376.
- [5] K. Osakada, M. Shiomi, Flexible manufacturing of metallic products by selective laser melting of powder, *Int. J. Mach. Tools Manuf.*, 46 (2006) 1188–1193.
- [6] J. Parthasarathy, B. Starly, S. Raman, A. Christensen, Mechanical evaluation of porous titanium (Ti6Al4V) structures with electron beam melting (EBM), *J Mech Behav Biomed Mater*, 3 (2010) 249–259.
- [7] H.N. Chia, B.M. Wu, Recent advances in 3D printing of biomaterials, *J. Biol. Eng.*, 9 (2015) 4.
- [8] J.P. Li, J.R. De Wijn, C.A. Van Blitterswijk, K. De Groot, The effect of scaffold architecture on properties of direct 3D fiber deposition of porous Ti6Al4V for orthopedic implants, *J. Biomed. Mater. Res. - Part A*, 92 (2010) 33–42.
- [9] E.Vidal, D.Torres, J. GuillemMarti, G. Sconti, J.M. Manero, M.P. Ginebra, D. Rodríguez, E. Rupérez, titanium Scaffolds by Direct Ink Writing: Fabrication and Functionalization to Guide Osteoblast Behavior, *Metals*, 10 (2020) 1156.
- [10] A. Civantos, E. Martinez-Campos, V. M. Ramos, C. Elvira, A. Gallardo, A. Abarategi, Titanium Coatings and Surface Modifications: Towards Clinically Useful Bioactive Implants, *ACS Biomater. Sci. Eng.*, 3 (2017) 1245-1261.
- [11] J. Guillem-Marti, N. Cinca, M. Punset, I. García, F.J. Gil, J. M. Guilemany, S. Dosta, Porous titanium-hydroxyapatite composite coating obtained on titanium by cold gas spray with high bond strength for biomedical applications, *Colloids Surfaces B Biointerfaces*, 180 (2019) 245–253.
- [12] G. Bezzi, G. Celotti, E. Landi, T.M.G. La Torretta, I. Sopyan, A. Tampieri, A novel sol-gel technique for hydroxyapatite preparation, *Mater. Chem. Phys.*, 78 (2003) 816–824.
- [13] S.V. Dorozhkin, Calcium orthophosphate coatings, films and layers, *Prog. Biomater.*, 1 (2012) 1.
- [14] Y. Abe, T. Kokubo, T. Yamamuro, Apatite coating on ceramics, metals and polymers utilizing a biological process, *J. Mater. Sci. Mater. Med.*, 1 (1990) 233–238.
- [15] F.J. García-Sanz, M.B. Mayor, J.L. Arias, J. Pou, B. León, M. Pérez-Amor, Hydroxyapatite coatings: A comparative study between plasma-spray and pulsed laser deposition techniques, *J. Mater. Sci. Mater. Med.*, 8 (1997) 861–865.
- [16] E. Vidal, J. Buxadera-Palomero, C.Pierre, J.M. Manero, M.P.Ginebra, S. Cazalbou, C. Combes, E.Rupérez, D. Rodriguez, Single-step pulsed electrodeposition of calcium phosphate coatings on titanium for drug delivery, *Surf. Coat. Technol.*, 358 (2018) 266-275.
- [17] H.X. Wang, S.K. Guan, X. Wang, C.X. Ren, L.G. Wang, In vitro degradation and mechanical integrity of Mg-Zn-Ca alloy coated with Ca-deficient hydroxyapatite by the pulse electrodeposition process, *Acta Biomater.*, 6 (2010) 1743–1748.
- [18] T. Li, L. Ling, M. Lin, H. Peng, H. Ren, Recent advances in multifunctional hydroxyapatite coating by electrochemical deposition, *J. Mater. Sci.*, 55 (2020) 6352-6374.
- [19] D. Gopi, J. Indira, L. Kavitha, A comparative study on the direct and pulsed current electrodeposition of hydroxyapatite coatings on surgical grade stainless steel, *Surf. Coatings Technol.*, 206 (2012) 2859–2869.
- [20] M.J. Liu, M. Zhang, X.F. Zhang, G.R. Li, Q. Zhang, C.X. Li, C.J. Li, G.J. Yang, Transport and deposition behaviors of vapor coatings materials in plasma spray-physical vapor

- deposition, *Applied Surface Science*, 486 (2019) 80-92.
- [21] M.P. Ginebra, C. Canal, M. Espanol, D. Pastorino, E. B. Montufar, Calcium phosphate cements as drug delivery materials, *Adv. Drug Deliv. Rev.*, 64 (2012), 1090–1110.
- [22] L. Zhao, P.K. Chu, Y. Zhang, Z. Wu, Antibacterial coatings on titanium implants, *J. Biomed. Mater. Res. - Part B Appl. Biomater.*, 91 (2009) 470–480.
- [23] M. Stigter, J. Bezemer, K. De Groot, P. Layrolle, Incorporation of different antibiotics into carbonated hydroxyapatite coatings on titanium implants, release and antibiotic efficacy, 9 (2004) 127–137.
- [24] A.A. Campbell, L. Song, X.S. Li, B.J. Nelson, C. Bottoni, E.S. DeJong, Development, characterization, and anti-microbial efficacy of hydroxyapatite-chlorhexidine coatings produced by surface-induced mineralization, *J. Biomed. Mater. Res.*, 53 (2000) 400–407.
- [25] J. Barros, L. Grenho, M.H. Fernandes, C. M. Manuel, L.F. Melo, O.C. Nunes, F.J. Monteiro, M.P. Ferraz, Anti-sessile bacterial and cytocompatibility properties of CHX-loaded nanohydroxyapatite, *Colloids Surfaces B Biointerfaces*, 130 (2015) 305–314.
- [26] C. Souza, A. Colombo, R. Souto, C. Silva-Boghossian, J. Granjeiro, G. Alves, A. Rossi, M.H. Rocha-Leão, Adsorption of chlorhexidine on synthetic hydroxyapatite and in vitro biological activity, *Colloids Surfaces B Biointerfaces*, 87 (2011) 310–318.
- [27] ISO 13314:2011. Mechanical testing of metals — Ductility testing — Compression test for porous and cellular metals.
- [28] C. Labay, J. Buxadera-Palomero, M. Avilés, C. Canal, M. P. Ginebra, Modulation of release kinetics by plasma polymerization of ampicillin-loaded  $\beta$ -TCP ceramics, *J. Phys. D. Appl. Phys.*, 49 (2016) 304004.
- [29] M. Hoyos-Nogués, F. Velasco, M. Ginebra, J.M. Manero, F.J. Gil, and C. Mas-Moruno, Regenerating bone via multifunctional coatings: The blending of cell integration and bacterial inhibition properties on the surface of biomaterials, *ACS Appl. Mater. Interfaces*, 9 (2017) 21618-21630.
- [30] I.M. Mehdawi, A. Young, Antibacterial composite restorative materials for dental applications, *Biomaterials and Medical Device - Associated Infections*, L.Barnes, I.R. Cooper, Ed. Woodhead Publishing, 2015, pp. 199-221.
- [31] C. Rey, O. Marsan, C. Combes, C. Drouet, D. Grossin, S. Sarda, Characterization of calcium phosphates using vibrational spectroscopies, *Advances in Calcium Phosphate Biomaterials*, Springer, Berlin, Heidelberg (2014), pp. 229-266.
- [32] R. Drevet, H. Benhayoune, Electrochemical deposition of calcium phosphate coatings on a prosthetic titanium alloy substrate, in *Calcium Phosphate: Structure, Synthesis, Properties, and Applications*, R. Heimann, Ed. Nova Science Publishers, 2012, pp. 231–252.
- [33] S.O.R. Sheykhosslami, J. Khalil-Allafi, L. Fathyunes, Preparation, Characterization, and Corrosion Behavior of Calcium Phosphate Coating Electrodeposited on the Modified Nanoporous Surface of NiTi Alloy for Biomedical Applications, *Metall. Mater. Trans. A*, 49 (2018) 5878–5887.
- [34] D.N. Da Rocha, M.H.P. Da Silva, J.B. De Campos, R.L.S.B. Marçal, D.Q. Mijares, P.G. Coelho, L.R. Cruz, Kinetics of conversion of brushite coatings to hydroxyapatite in alkaline solution, *Journal of Materials Research and Technology*, 7 (2018) 479–486.
- [35] J. Fornell, Y.P. Feng, E.M. Pellicer, M.D. Baró, S. Suriñach, J. Sort, Mechanical behaviour of brushite and hydroxyapatite coatings electrodeposited on newly developed FeMnSiPd alloys, *J. Alloys Compd.*, 729 (2017) 231–239.
- [36] D.Gopi, J. Indira, L. Kavitha, A comparative study on the direct and pulsed current electrodeposition of hydroxyapatite coatings on surgical grade stainless steel, *Surf. Coatings Technol.*, 206 (2012) 2859-2869.
- [37] Z. Z. Fang, Ed., *Sintering of advanced materials: Fundamentals and processes*, first ed., Woodhead Publishing Limited, 2010.
- [38] H. Danninger, R.D.O. Calderon, C. Gierl-Mayer, *Powder Metallurgy and sintered Materials*, Ullmann's Encyclopedia of Industrial Chemistry, 2017.

- [39] E.F. Morgan, G.U. Unnikrisnan, A.I. Hussein, Bone mechanical properties in healthy and diseased states. *Annu. Rev. Biomed. Eng.*, 20 (2019) 119–143.
- [40] H. Ketata, F. Affes, M. Kharrat, M. Dammak, A comparative study of tapped and untapped pilot holes for bicortical orthopedic screws – 3D finite element analysis with an experimental test, *Biomed. Eng.-Biomed. Tech.*, 64 (2019) 563–570.
- [41] D.A.C. Heesterbeek, N.I. Martin, A. Velthuisen, M. Duijst, M. Ruyken, R. Wubbolts, S.H.M. Rooijackers, B.W. Bardoel, Complement-dependent outer membrane perturbation sensitizes Gram-negative bacteria to Gram-positive specific antibiotics, *Sci Rep*, 9 (2019) 3074.
- [42] M. Giannelli, F. Chellini, M. Margheri, P. Tonrlli, A. Tani, Effect of chlorhexidine digluconate on different cell types: a molecular and ultrastructural investigation, *Toxicol In Vitro*, 22 (2007) 308–317.
- [43] Y. Su, I. Cockerill, Y. Zheng, L. Tang, Y. Qin, D. Zhu, Biofunctionalization of metallic implants by calcium phosphate coatings, *Bioact. Mater.*, 4 (2019) 196–206.
- [44] L. Damiati, M.G. Eales, A.H. Nobbs, B. Su, P.M. Tsimbouri, M. Salmeron-Sanchez, M.J. Dalby, Impact of surface topography and coating on osteogenesis and bacterial attachment on titanium implants, *J. Tissue Eng.*, 9 (2018) 1–16.
- [45] M. Gimeno, P. pinczowski, M. Pérez, A. Giorello, M.A. Martínez, J. Santamarí, M. Arruebo, L. Luján, A controlled antibiotic release system to prevent orthopedic-implant associated infections: An in vitro study, *Eur. J. Pharm. Sci.*, 96 (2015) 264–271.
- [46] N.A. Peppas, Analysis of Fickian and non-Fickian drug release from polymers, *Pharm. Acta Helv.*, 60 (1985) 110–111.
- [47] R.W. Kormsmeier, R. Gurny, E. Doelker, P. Buri, N.A. Peppas Mechanisms of solute release from porous hydrophilic polymers, *Int. J. Pharm.*, 15 (1983) 25–35.
- [48] H. Noukrati, S. Cazalbou, I. Demnati, C. Rey, A. Barroug, C. Combes, Injectability, microstructure and release properties of sodium fusidate-loaded apatitic cement as a local drug-delivery system, *Mater. Sci. Eng. C*, 59 (2016) 177–184.
- [49] P. Costa, J.M. Sousa Lobo, Modeling and comparison of dissolution profiles, *Eur. J. Pharm. Sci.*, 13 (2001) 123–133.
- [50] G.R. Biswas, S. B. Majee, Modeling of drug-difusion kinetics of amoxicillin trihydrate from buccal tablets, *Int. J. Pharm. Bio Sci.*, 6 (2015) 859–866.
- [51] S. Ghosh, V. Wu, S. Pernal, and V. Uskokovic, Self-Setting Calcium Phosphate Cements with Tunable Antibiotic Release Rates for Advanced Antimicrobial Applications, *ACS Appl. Mater. Interfaces*, 8 (2016) 7691–7708.

## Supplementary information

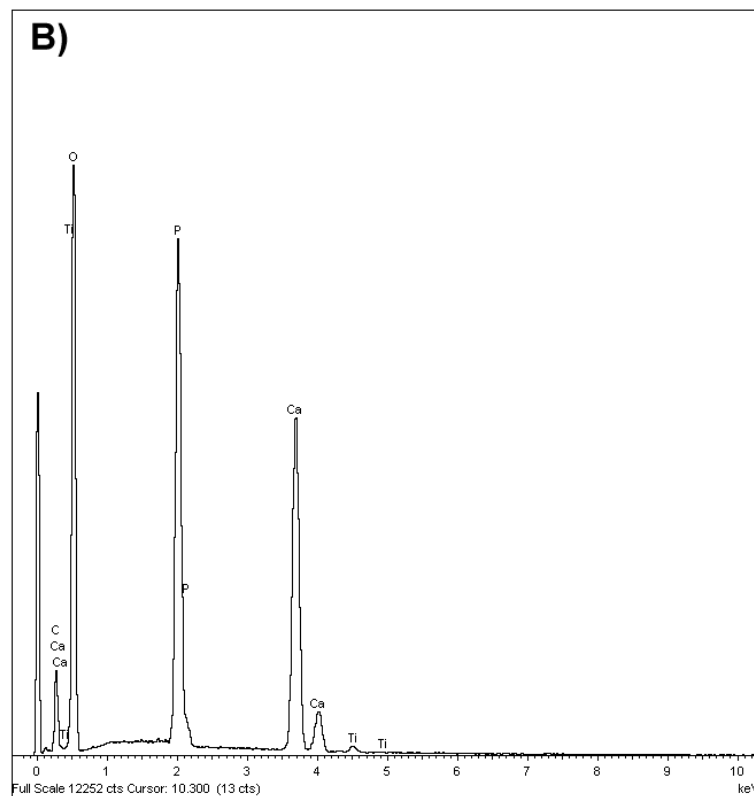
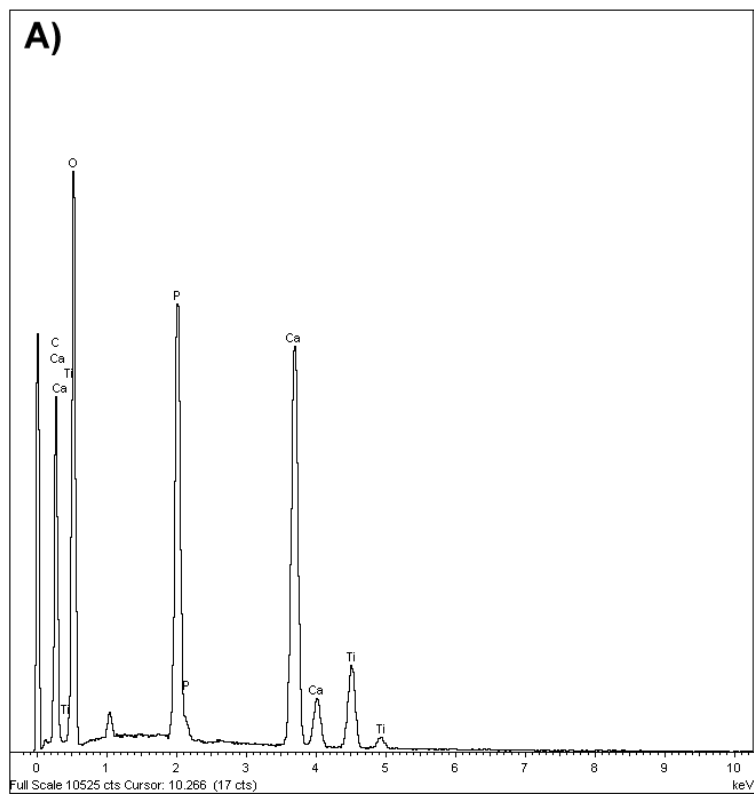


**Figure S1.** Spectrum of EDX spot analysis at: A) Point 1 of Figure 2C, B) Point 2 of Figure 2C.

**Table S1.** EDX semi-quantitative analysis (at. %) of the spectra shown in Figure S1.

| <b>Spectrum</b> | <b>C</b> | <b>O</b> | <b>P</b> | <b>Ca</b> | <b>Ti</b> | <b>Total</b> | <b>Ca/P ratio</b> |
|-----------------|----------|----------|----------|-----------|-----------|--------------|-------------------|
| Point 1         | 29.29    | 51.29    | 7.17     | 9.29      | 2.96      | 100.00       | 1.30              |
| Point 2         | 14.24    | 61.51    | 12.31    | 11.64     | 0.30      | 100.00       | 0.95              |

All elements analyzed (Normalized)